CRYSTAL GROWTH & DESIGN

Article

pubs.acs.org/crystal

Image-Analysis-Based Method for 3D Crystal Morphology Measurement and Polymorph Identification Using Confocal Microscopy

Meenesh R. Singh,[†] Jayanta Chakraborty,[‡] Nandkishor Nere,[§] Hsien-Hsin Tung,[∥] Shailendra Bordawekar,[∥] and Doraiswami Ramkrishna*,[†]

[†]Chemical Engineering Department, Purdue University, 480 Stadium Mall Drive, West Lafayette, Indiana 47907, United States

[‡]Chemical Engineering Department, Indian Institute of Technology Kharagpur, Kharagpur, West Bengal 721302, India

[§]Process Engineering & Sciences, Adiya Birla Science & Technology Company Ltd., Plot No. 1 & 1-A/1, MIDC Taloja, Tal. Panvel, Dist. Raigad, Maharashtra 410208, India

[∥]Process Engineering, Global Pharmaceutical R&D, Abbott Laboratories, 1401 Sheridan Road, North Chicago, Illinois 60064, United States

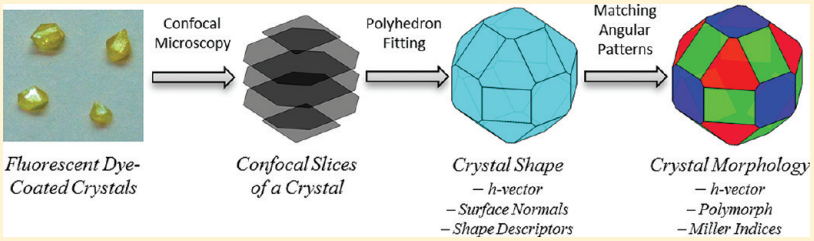

ABSTRACT: A new technique for the measurement of 3D crystal morphology and identification of its polymorph using tomographic images is proposed. Confocal microscopy is used for the first time to obtain tomographic images of crystals that are coated with a suitable fluorescent dye. A convex polyhedron is fitted through a stack of tomographic images of a crystal to obtain the normal vectors of each facet and their corresponding perpendicular distances from the center of the crystal. The angular patterns are generated from the measured normal vectors and are matched with the master angular patterns of each polymorph. It is shown that the matching of the angular patterns is unique and provides a simpler way to identify polymorphs. An image-analysis program that can be integrated with conventional confocal microscopes was created to sequentially perform image processing, morphology measurement, and polymorph detection. This program was used to measure morphologies and identify polymorphs of 2D and 3D acetaminophen crystals. Detailed directions are provided to enable the application of the methodology without the need for special-purpose software. The image-analysis program is also suitable for repeated measurements to produce morphology distributions. This technique will provide an effective platform for measuring the 3D shapes of materials of interest to many applications.

1. INTRODUCTION

Measurement of crystal morphology is of high interest in current research on crystalline material for diverse industrial applications. Widely used techniques to measure crystal morphology are based on microscopy and digital video imaging. Such techniques rely on an appropriate method of image acquisition followed by a suitable image-analysis scheme to extract morphological details. Researchers have used stereoscopic imaging and model-based shape recognition to measure simple crystal shapes such as parallelepipeds and cubes. However, a technique for the comprehensive measurement of complex crystal shapes does not exist. We present herein evidence of a new, strikingly simple, and inexpensive method for identifying complex crystal shapes and polymorphs through computer-aided analysis of tomographic images produced with a confocal microscope.

Real-time visualization of complex processes offers the best prospects for understanding their intricate behavior by revealing essential features. A broad class of such processes associated with the pharmaceutical industry includes crystallization, milling, and granulation, which are inherently complex and difficult to control. Moreover, the successful design and implementation of control strategies for such processes depend strongly on robust and efficient techniques to monitor their behavior. In crystallization, the simultaneous occurrence of particulate events such as nucleation, breakage, and aggregation provides for an even more complex setting to monitor and control the properties of crystalline products. Consequently, the application of multiple sensors for dynamic measurements of crystal properties such as size, shape, and polymorph has evolved in industrial crystallization.

The most commonly used instruments for online measurement of particle size distributions are based on either light scattering or imaging, for example, focused-beam reflectance measurement (FBRM) and particle vision measurement (PVM) probes. Raman-scattering- and X-ray-diffraction-based detectors are

Received: April 20, 2012
Revised: May 25, 2012
Published: May 28, 2012

widely used for online measurement of polymorph content. These measurement techniques can, however, provide only crude information on particle shapes such as sphericity, aspect ratio, and equivalent diameters, thus presenting a dire need for better techniques to measure crystal shape and related properties. The objective of this article is to present a new image-analysis-based method for the measurement of three-dimensional (3D) crystal morphology, polymorphs, and morphology distributions.

The term "morphology" normally refers to the detailed description of an object, but in the current context, it simply means "external shape with respect to crystallographic axes". Morphology is an important attribute of a crystalline material that affects not only downstream processes (such as filtration, washing, granulation, drying, grinding, transportation, storage, and tableting) but also end-use properties (such as bulk density, mechanical strength of a tablet, catalytic activity, stability, wettability, and flowability). Crystals of desired morphology can be produced through (i) theoretical understanding of how suitable crystals can be grown in an industrial crystallizer and (ii) adequate analytical tools for measuring morphology distributions of crystal products. The former issue has received considerable attention in the past through the development of mathematical models toward predicting crystal morphology distributions. Clearly, the validation of such models must be based on the development of experimental techniques providing for observations to match the model predictions. Because of the lack of adequate experimental tools for measuring the morphologies of 3D crystals, the applicability of morphological models has been limited only to crystals that can be approximated as two-dimensional (2D) objects. Although this article is predicated on the use of confocal microscopy, the theoretical development is a new instrument-independent, image-analysis-based methodology with the potential for online measurement of morphology distributions and detection of polymorphs.

The image-analysis program should act as an interface for deciphering images to some shape-related quantity that must be defined in a unique and simple way. A few mathematical descriptors that are used to define the shapes of geometric objects are Fourier descriptors,[1] fractals,[2] Minkowski functionals,[3] curvatures, [4] and polynomials.[5] A review of various shape descriptors and shape-analysis techniques for different applications can be found elsewhere.[6] For the simple case of a single crystal that can be viewed as a convex polyhedron, the shape can be conveniently described by a set of perpendicular distances (**h**, which we refer to as the h vector) of its faces (or planes) from the origin. The set of perpendicular distances (h vector) along the directions of the normals to the crystal faces (or Miller indices) constitutes the crystal morphology. This representation of crystal morphology, which is due to J. W. Gibbs and was the first to provide thermodynamic reasoning for the equilibrium form of a crystal shape, has the following two advantages: First, the dynamic behavior of the h vector can be directly related to well-established crystal growth models (such as 2D nucleation, spiral growth, and rough growth), and second, the h vector can be easily studied for the polyhedral symmetry of a crystal.

The dynamics of crystal morphology distributions (or h vector distributions) is usually formulated using population balance equations (PBEs) in terms of h vectors.[7,8] Recent advances in numerical techniques[9] and methodologies to reduce the computational load[10] associated with PBEs have made it feasible to simulate the evolution of crystal morphology distributions. However, such a detailed description of crystal morphology has problems with its measurements, as conventional light-scattering devices

Table 1. List of Crystal Shape-Measurement Techniques

class of techniques	examples	advantages	limitations
behavioral systems	inclined rotating disk[17] and cylinder,[18] sieve cascadograph[19]	easy to separate particles based on shape and size; some information provided on distribution of shape descriptors	cannot provide details of single-particle shapes; shape description depends on the type of physical process
light scattering	dynamic light scattering (DLS),[20] focused-beam reflectance measurement (FBRM)[21]	DLS can yield particle size distributions (PSDs) and average equivalent sizes; FBRM usually used for online measurements of chord length distributions (CLDs)	cannot measure PSDs; CLDs measured using FBRM are often biased because of particle-shape effects associated with orientation
interferometry[22]	Mach–Zehnder,[23] Michelson, Fabry–Pérot, Sagnac, common-path, fiber interferometry	great potential for nondestructive and online measurements of surface topography; vertical resolution can be as small as 1 nm	cannot be used to measure crystal shapes; can realize the surface roughness up to $\lambda/2$
X-ray diffraction	single-crystal X-ray diffraction[24]	can precisely measure single-crystal shapes	large time and data-processing requirements; extremely difficult to measure shapes of many crystals
stereoscopic imaging	stereoscopic particle image velocimetry (PIV),[25] multiple-camera-based techniques[26,27]	extremely useful for measuring shape distributions of symmetric crystal shapes such as cuboids and ellipsoids; very well-established for online measurements	difficult to obtain shape distributions for complex shapes; often limited by poor resolution of video camera and insufficient light exposure
optical sectioning/tomography	confocal microscopy,[28] X-ray microscopy[29]	sharp vertical resolution enables thin slices of crystal, which can be reconstructed to yield 3D shapes	tradeoff required between number of slices captured and time of operation
projection-based	optical microscopy,[30] transmission electron microscopy (TEM),[31] process vision and measurement (PVM)[32]	frequently used for 2D crystals; TEM can provide high resolution; PVM usually used for online monitoring	difficult to obtain shapes of 3D crystals; surface topography can be realized using differential interference contrast (DIC) or stage tilting
high-depth-of-field microscopy	scanning tunneling microscopy (STM),[33] atomic force microscopy (AFM),[33] scanning electron microscopy (SEM)[34]	high vertical resolution allows accurate measurement of surface topography	require confined environment and significant sample preparation time; can provide only surface topography

can yield only equivalent sizes but not shapes (or h vectors). Because of the limitations of the many other techniques listed in Table 1, we envisage the use of confocal microscopy or related techniques (such as multiphoton microscopy and X-ray microscopy) to take the cross-sectional images of crystals and process them using our image-analysis technique to obtain crystal morphologies, polymorphs, and morphology distributions. The proposed technique relies on extracting the most information from the crystal images that can be translated to any shape descriptors used industry-wide. It further has the potential for online measurements, when combined with an appropriate setup for continuous feeding of dye-coated crystals to a microscope and automatic adjustment of the focus.[11−13]

The organization of this article is as follows: Section 2 discusses various techniques that have been used in the past for crystal morphology measurement and polymorph detection. Section 3 describes our image-analysis methodology for the measurement of crystal morphology with an algorithm for Miller index identification and polymorph detection. Section 4 discusses the methods used to prepare and image samples. Section 5 demonstrates the image-analysis technique using in silico generated images and real images of acetaminophen obtained from a confocal microscope. Finally, some conclusions are presented in section 6 about the methodology, outlining the future scope of the proposed technique for online measurements.

2. PREVIOUS WORK

Shape-measurement techniques can be broadly classified as direct or indirect methods. Direct methods encompass all imaging techniques that are based on either microscopy (using a stylus or electromagnetic radiation) or interferometry. These techniques usually employ some image-analysis software that reads, analyzes, and quantifies images. The high spatial resolution, accuracy, and robustness of such optical techniques have confirmed their worth for online measurement of surface topography[14] and tracking of particle motion.[15] An overview of methods used to measure three-dimensional surface topography can be found elsewhere.[16] Conversely, indirect methods make use of behavioral systems to study the effect of shape on particle dynamics and extract shape descriptors by solving the inverse problem.

A brief list of the most commonly used techniques to measure particle shape or shape distribution is presented in Table 1, although this list is not intended to be exhaustive. The remainder of this section preovides a short review of the development of shape-measurement techniques in crystal research.

2.1. Behavioral Systems and Shape Descriptors. The measurement of crystal morphology is of paramount importance for the design and implementation of strategies for the controlled production of crystalline materials. A primitive approach in the past to inferring crystal morphology was to examine some specific shape-dependent behavior. For example, the rolling tendency of powder in an inclined rotating disk or cylinder and the residence time distribution in sieve cascadograph were used for extracting shape descriptors.[17−19] Shape descriptors are scalar quantities that are sensitive to the crystal shape. Although such shape descriptors are only indicators and not a full description of crystal shapes, they have been used in one form or another for controlling product quality in industrial practice. Consequently, shape descriptors have gained tremendous applications in manufacturing industries following the advent of imaging techniques for their direct measurement. The selection of shape descriptors is critical, as the descriptors must be invariant to the orientation of the object.[35] Shape descriptors can be classified as macroshape and mesoshape descriptors based on the details required for particle shape description. Macroshape descriptors can be calculated from measurements made on particle image (e.g., form factor, roundedness, aspect ratio, elongation), whereas the mesoshape descriptors are obtained from the comparison of a real particle with some reference shape such as a convex polygon.[36] Also, shape-descriptor measurements are highly sensitive to details of the image-acquisition procedures such as image magnification, lighting technique, and number of particles measured.[37]

2.2. Imaging Instruments: Inline, Online, and Offline. The rapid advancement in image-acquisition and -processing technologies has led to the possibility of real-time measurements of morphology evolution in industrial crystallizers. Various inline imaging probes are commercially available such as Particle Imaging System (PARIS) of DuPont, Particle Vision and Measurement (PVM) of Lasentec and Mettler Toledo Ltd., Process Image Analyzer (PIA) of MessTechnik Schwartz GmbH, and In Situ Particle Viewer (ISPV) of Perdix Analytical Systems.[38] Endoscopy−stroboscopy imaging sensors such as ATMOS endoscopic systems represent some of the recent inline imaging instruments (originally used for medical diagnosis) capable of monitoring the color, transparency, size, and shape of pharmaceutical crystals.[39] These invasive instruments are based on borescopes with a strobe light source and a video camera mounted on one end to capture images inside crystallizers. Although such imaging probes are flexible, fast, and robust, they are prone to poor visibility arising from particle clogging and increasing particle density inside the crystallizer. Particle clogging of sensors can be avoided by using noninvasive schemes for online measurement of crystal morphology. Examples of two such noninvasive schemes are the stroboscopic video imaging system of GlaxoSmithKline[40] and hot-stage optical microscopy.[27] The former takes online images from the exterior of a crystallizer, and the latter takes online images of crystals that are continuously supplied to the hot stage and recycled back to the crystallizer. Stroboscopic video imaging is also affected by background noise due to improper lighting, high particle density, and particle motion effects. However, better images can be obtained using optical microscopy by adjusting light intensity, diluting particle slurries, and stopping slurry flow. The offline imaging techniques reported in Table 1 such as stereoscopic video imaging,[41] scanning electron microscopy (SEM),[34] and atomic force microscopy (AFM)[33] are also frequently used to analyze crystalline materials obtained after drying samples taken from crystallizers. Other offline PAT imaging systems include Sysmex FPIA-3000, Pharma-Vision System (PVS), and Morphologi G3 of Malvern Instruments. Such in situ imaging techniques are mostly limited by their capability to capture two-dimensional images of crystals. Therefore, they are assisted with some image-analysis tools to approximate three-dimensional features of crystals, as discussed later. Some of the three-dimensional (3D) imaging techniques such as confocal, multiphoton, and X-ray microscopy are based on the principles of tomography to take optical slices of a crystal and reconstruct its 3D shape using image analysis. Among these techniques, confocal microscopy has emerged as a powerful tool for the dynamic measurement of 3D structures of biological samples[28] and solid surfaces.[42] Some of the features that make it an attractive technique are high resolution of approximately 200 nm and high scanning speed on the order of 1 s per image, although these features might vary depending on the type of sample. Nevertheless, it is a promising technique for dynamic measurements with the potential for online

adaptability.[13] This article demonstrates the use of confocal microscopy to acquire 3D images of crystals that are further processed using a unique image-analysis algorithm presented herein to obtain crystal morphologies and polymorphs.

2.3. Image Processing and Analysis. Any imaging system has three basic elements, namely, capture, curation, and analysis. We previously discussed different techniques normally used to capture images, which are further processed for shape measurements using an image-analysis program that performs the other two elements (curation and analysis). Curation is a preliminary process of any image-analysis program that basically prepares images for the measurement of their features and performs measurements. It has two major components: image enhancement and image segmentation. Image enhancement involves techniques such as gray-level histogram modification, smoothing, and sharpening to improve the visual appearance of an image for better machine interpretation, whereas image segmentation uses an appropriate thresholding algorithm such as global thresholding, local binarization, and watershed transforms to create a binary image (or to separate an object from the background).[43] A different class of image segmentation technique, called multivariate image analysis, involves performing multiway principal component analysis to decompose highly correlated data in images.[39,44] After the curation of an image and its transformation to binary form have been completed, appropriate analysis can be performed for the measurement of relevant features. Some examples of basic analyses are measurements of length, width, circularity, convexity, and Ferret diameter. However, a few advanced analysis algorithms such as Camera Model[45] and Model-Based Shape Recognition for Crystals (M-SHARC)[46] have also been developed to identify the shapes of crystals. Such models are based on creating a library of 2D projection of crystal shapes at different orientations and determining crystal shape by identifying projected images from the library. Clearly, these models are questionable for the case of asymmetric crystals with large numbers of faces, as the identification of a unique crystal shape for some projected images is not assured. The main focus of this article is the development of an image-analysis program for tomographic images to derive complete morphological and polymorphic details for crystalline materials.

3. NEW TECHNIQUE FOR CRYSTAL MORPHOLOGY MEASUREMENT AND POLYMORPH DETECTION

The ability of crystallization processes to produce products of desired qualities relies on the availability of appropriate measurement and analysis tools. The rigor required in image analysis must be commensurate with the quality of images obtained from the imaging instrument. An instrument producing images with poor resolution and/or significant background noise will increase the image-processing time, which can be reduced or avoided by properly selecting/tuning imaging instruments to yield improved images. The image-analysis technique presented herein takes tomographic images from a confocal microscope with high resolution and low background noise, thus obviating the need for advanced image-processing techniques. Section 3.1 discusses the algorithm for measuring 2D crystal shapes using projected images of crystals by fitting a convex polygon. Then, section 3.2 extends the same idea to measure the shape of a 3D crystal by fitting a convex polyhedron. Subsequently, section 3.3 deals with the identification of the Miller indices of crystal faces and thereby deciphering the crystal's polymorph. The conversion of a measured shape quantity, *h* vector, to other easily measurable quantities such as sphericity, aspect ratio, anf equivalent diameters is shown in section 3.4. The structure of the image-analysis program with different modules is described in section 3.5.

3.1. Measurement of 2D Crystal Morphology. Some crystals have a tendency to attain a variety of 2D shapes, needle or platelike, under different operating conditions and are referred to as 2D crystals because they are relatively small in at least one direction. Examples of industrially grown 2D crystals with applications in the pharmaceutical, semiconductor, and catalyst industries are L-glutamic acid, succinic acid, hen-egg-white lysozyme, CdSe nanorods, and TiO nanosheets. It is essential to have appropriate tools to measure morphology distributions, which, in this case, could be any one of the projection-based techniques listed in Table 1, for the production of crystals with shape-controlled properties. Projection-based techniques such as optical microscopy and video microscopy take images of crystal projections, recording their 2D shapes only with no information on thickness. Nevertheless, these techniques provide nearly complete shape descriptions, as the relative thickness is almost unchanged during the course of crystallization. The captured images of crystal projections are processed to remove noise, enhance contrast, and prepare them for analysis.

The typical outcome from image processing is binary (black-and-white) image that is further processed by an image-analysis algorithm as shown in Figure 1 to obtain the *h* vector of any 2D crystal. The following five steps are involved in the algorithm for determining the shape of a 2D crystal.

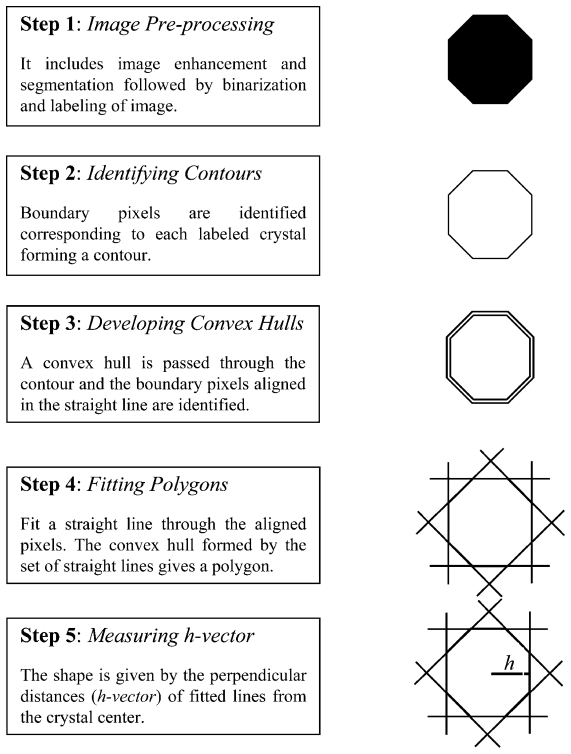

Figure 1. Image algorithm to measure the shapes of 2D crystals with an illustrative treatment of an octagon.

Step 1. The images are prepared for analysis by performing some or all of the image-processing steps listed in section 2.3. The extent of processing required is inversely related to the quality of the images. Therefore, the time required in this step can be minimized by careful operation of the imaging instruments (for example, supplying sufficient light exposure, properly choosing lens and focus). The preprocessed image is converted

to a binary form, and each crystal in the image is labeled to facilitate identification and perform simultaneous analysis.

Step 2. The usual binary representation of the image after step 1 is such that crystals are colored black and background is white. The collection of black pixels at the interface of the crystal and background forms a contour of the crystal. These boundary pixels can be easily identified using Matlab subroutine imcontour.

Step 3. This part of the algorithm identifies those pixels of the contour that are lying on a straight line. There are many ways of finding straight lines in intensity images; one popular approach is to group pixels corresponding to similar intensity gradients.[47] Here, we use a relatively simple technique of finding pixels on straight lines using a convex hull. Specifically, to obtain convex hulls, we used the Quickhull algorithm,[48] which is available in Matlab as the subroutine convhulln and whose outputs are the indices of pixels comprising facets of the convex hull.

Step 4. The straight lines are fit through the set of pixels comprising facets of a crystal by linear regression. For example, step 4 in Figure 1 shows the fitting of eight straight lines passing through each face of the octagon, which coincides with the smallest convex region. The output from this step is a set of linear equations of the form $a_i x + b_i y = d_i$, corresponding to each face of the crystal, with respect to some center.

Step 5. The h vector can be directly obtained from the set of linear equations by calculating the perpendicular distances (h) of the straight lines from some appropriate point inside the crystal.

This algorithm works very well with 2D faceted crystals, and its performance on real crystals is demonstrated in section 5.1. Although this approach can be extended to nonfaceted crystals (for example, by fitting analytic functions, such as Fourier series or polynomial functions, to boundary pixels), we restrict consideration to only faceted crystals because of the complexity associated with modeling the shape evolution of nonfaceted crystals. Consequently, the proposed algorithm is expected to be useful for validating such models and can also be used independently in different applications to measure the shapes of 2D crystals.

3.2. Measurement of 3D Crystal Morphology. Crystals grown in crystallizers can take varieties of shapes, ranging from needlelike to more complex polyhedral shapes, based on operating conditions and material properties. The measurement of crystal shapes is of critical importance for the controlled synthesis of crystalline products with desired physical attributes. As discussed in section 2, many light-scattering- and imaging-based techniques can be used to infer crystal shapes in some approximate ways. Although some techniques such as single-crystal X-ray diffraction, X-ray tomography, confocal microscopy, and multiphoton microscopy can capture shapes of crystals more precisely than others, their applications in quantifying shape distributions are limited because of the unavailability of an appropriate framework that can read images and quantify shape distributions. This section presents a new methodology for obtaining the complete shape description (in terms of the h vector and corresponding normal vectors) from tomographic images of a faceted crystal.

Tomographic images are actually a set of cross-sectional images of crystals that can be obtained from instruments such as confocal microscopes. These images are processed with a method similar to that described earlier for 2D crystals and converted into binary images for further analysis using the algorithm shown in Figure 2, to obtain the h vector and normal vectors for any 3D crystal. The image-analysis algorithm for 3D crystals is the same as for 2D crystals, except for the stack of images being processed and analyzed together to yield the 3D shape.

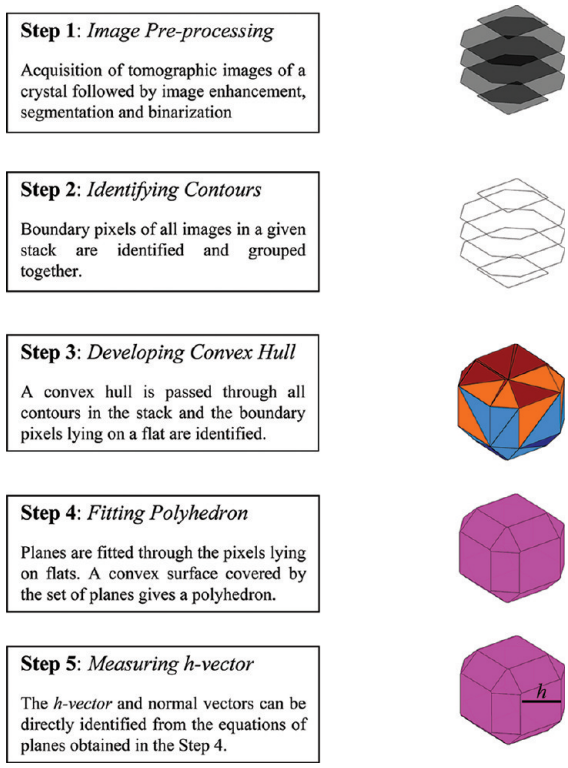

Figure 2. Image algorithm to measure the shapes of 3D crystals with an illustrative treatment of an icosahexahedron.

Step 1. All images in a stack are preprocessed and binarized. The information on the distance between two images in a given stack is known from the imaging instrument and is kept fixed throughout the analysis.

Step 2. The boundary pixels for all images in a stack are identified using the Matlab subroutine imcontour on each image in the stack. The resulting form is the set of level curves of the crystal.

Step 3. The set of boundary pixels corresponding to the entire stack is processed through the Matlab subroutine convhulln to yield a convex set of triangular faces (see Figure 2, step 3) covering all boundary pixels. It might be possible to obtain multiple triangular faces with nearly same orientations. Therefore, the triangular faces having the same orientations are grouped together, with each group forming a crystal face with a distinct orientation.

Step 4. The boundary pixels lying closest to a group of triangular faces (representing a facet of the crystal with a unique orientation) are identified, and the equation of a plane is fitted through these boundary pixels by linear regression.

Step 5. The set of equations corresponding to each face of the crystal can be used to calculate perpendicular distances (h vector) of the crystal faces from some center inside the crystal. The final outputs from this image-analysis program are the h vector and the corresponding normal vectors of the crystal faces, from which the crystal shape can be readily constructed.

It is worth noticing that the choice of center governs the number of distinct h values in the h vector that eventually reflects the symmetry of the crystal. This issue is addressed in the next section, and a method for deriving the center

corresponding to the maximum symmetry of the crystal from the crystal morphology is presented.

3.3. Crystal Face Recognition and Polymorph Detection. The shape of a crystal alone, without any reference to the atomic structure on crystal faces, is meaningless because the surface energetics and related properties cannot be defined uniquely. The shape-related properties can be determined uniquely only if the shape is defined with respect to crystallographic coordinates. The crystallographic coordinates are defined based on the shape of a unit cell of a crystal. The dimensions of a unit cell are known as lattice parameters and comprise the angles made by crystallographic axes (α, β, γ) and the lengths of the sides of a unit cell (a, b, c). Hence, a crystal can be viewed as an object with repeating arrangement of unit cells along crystallographic axes.

The shape of crystals relative to the crystallographic coordinates is referred to here as the morphology, whereas the polymorphs are characterized by the lattice parameters. To clarify further, crystals with identical polymorphs can have different growth morphologies, whereas the converse is not true. Measurements of crystal morphologies and polymorphs are of critical importance in assessing the quality of crystalline products. Different techniques can be used to measure shapes and polymorphs of crystals; however, there are no such techniques, except for X-ray microscopy and single-crystal X-ray diffraction (XRD), that can measure the morphologies of crystals. Single-crystal XRD can be used to determine the morphology of a single crystal, but it is time-consuming and impractical for use for a population of crystals.

The identification of crystal morphology requires the measurement of h vector and the assignment of Miller indices to the corresponding faces. For any instrument to be capable of measuring crystal morphology, it must be able to measure 3D shapes and detect crystallographic planes on crystal surfaces. We propose a simple, effective, and noninvasive method for detecting crystallographic planes from only the shape measurements.

A perfect crystal with a regular three-dimensional arrangement of atoms has constant interfacial angles irrespective of its shape. This was discovered by Nicolas Steno in 1669 and is known as Steno's law of constancy of interfacial angles: The angles between corresponding faces on crystals are the same for all specimens of the same mineral. It follows from Steno's law that all growth morphologies of crystalline materials with a fixed polymorphic form have identical and unique patterns of interfacial angles. Consequently, it can be stated that one polymorph differs from another by its interfacial angular patterns. Also, the interfacial angular pattern made by a face (belonging to some crystallographic family) with all other faces on a crystal is constant and unique for that family of faces. There exists a signature angular pattern for each family of planes in a given polymorph, and the set of angular patterns corresponding to all families of planes is unique for a given polymorph.[49]

The determination of polymorphs and the Miller indices of planes requires the construction of master angular patterns for energetically favorable faces that might appear during growth. Theoretically, a crystal has infinitely many planes, but only a few can appear during crystal growth. Bravais–Friedel–Donnay–Harker (BFDH) law is the basic way of selecting crystal that are likely faces to appear. It states that the larger a face's interplanar spacing (d_{hkl}), the slower its growth, and the greater its size. It accounts for the internal structure and symmetry of the crystal but not the attachment energy between atoms or molecules (growth units). Subsequently, Bennema and co-workers extended Hartman–Perdok (HP) theory to determine energetically favorable crystal faces. They proposed a methodology based on crystal graphs (prepared by growth units connected with noncovalent bonds) and connected net theory to determine low-energy (favorable, F) faces with more than one connected net. The connected-net analysis reduces crystal faces to a limited number. Boerrigter et al.[50] showed through connected-net analysis that crystal faces of monoclinic paracetamol such as {001},{011},{110}, and {201} are energetically more favorable to appear, in agreement with the experimental morphologies observed by Ristic et al.[51]

Consider a crystal with n energetically favorable planes constituting f families. The total number of planes and the corresponding normal vectors are written as

$$n = \sum_{i=1}^{f} m_i, \qquad \mathbf{N} = \begin{bmatrix} \mathbf{n}_1^{\mathrm{T}} \\ \mathbf{n}_2^{\mathrm{T}} \\ \vdots \\ \mathbf{n}_n^{\mathrm{T}} \end{bmatrix} \tag{1}$$

where m_i is the number of planes in the ith family and $\mathbf{N}$ is the matrix of normal vectors $\mathbf{n}_i$. The angular patterns $\boldsymbol{\theta}_j$ made by the jth face with all faces of the crystals are given as

$$\theta_{i,j} = \cos^{-1}(\mathbf{n}_i \cdot \mathbf{n}_j), \qquad i, j = 1, 2, \ldots, n \tag{2}$$

where angles in $\boldsymbol{\theta}_j = \{\theta_{i,j}\}_{i=1}^{n}$ are arranged in ascending order. It can be readily observed that all angular patterns in the ith family are the same, that is, $\boldsymbol{\theta}_{1,i} = \boldsymbol{\theta}_{2,i} = \ldots = \boldsymbol{\theta}_{m_i,i}$. The polymorph is uniquely characterized by its angular patterns $\{\boldsymbol{\theta}_j\}_{i=1}^{n}$, which are referred to here as the master angular patterns. These master angular patterns are compared with the experimentally measured angular patterns to identify polymorphs and assign Miller indices to crystal faces.

The algorithm for identifying polymorphs and assigning Miller indices to crystal faces is presented in Figure 3.

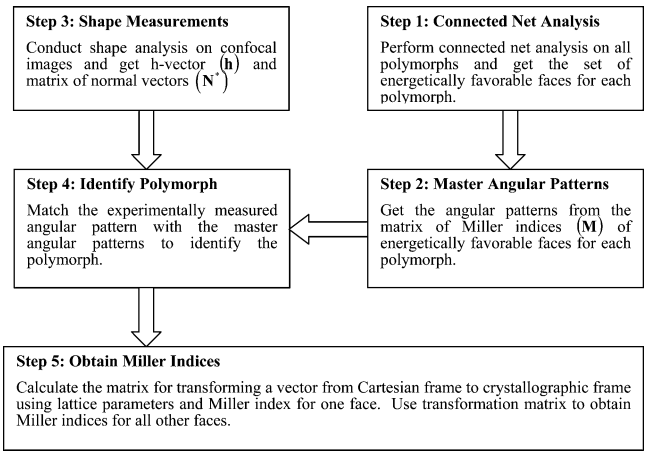

Figure 3. Algorithm for the identification of polymorphs and Miller indices of crystal faces from crystal shape information.

Step 1. The algorithm generates the set of energetically favorable faces (F faces) for a given polymorph. The method to identify F faces is well-established in the literature and is known as connected-net analysis.[50] For example, the F faces for acetaminophen are given in the Appendix. The set of Miller indices

(*hkl*) corresponding to F faces of a given polymorph are composed as rows in a matrix **M**.

Step 2. The row vectors $\mathbf{m}_j$ of **M** are the normal vectors of the F faces whose "components" are expressed in terms of the crystallographic frame of reference. They can be transformed into the vectors in the Cartesian frame using the transformation matrix **K**[52]

$$\mathbf{K} = \begin{bmatrix} a\omega_1 & 0 & 0 \\ a\omega_2 & b\sin\alpha & 0 \\ a\cos\beta & b\cos\alpha & c \end{bmatrix}^{-1} \tag{3}$$

where

$$\omega_1 = (1 - \cos^2\alpha - \cos^2\beta - \cos^2\gamma + 2\cos\alpha\cos\beta\cos\gamma)^{1/2}/\sin\alpha$$

$$\omega_2 = \frac{\cos\gamma - \cos\alpha\cos\beta}{\sin\alpha}$$

The transformation matrix **K** in eq 3 corresponds to the specific relative orientation of the crystallographic and Cartesian frames of references; specifically, the *c* axis (crystal frame) is parallel to the *z* axis (Cartesian frame), and the *b* axis (crystal frame) is in the *y*−*z* plane (Cartesian frame). The transformed normal vectors in the Cartesian frame can be obtained as

$$\mathbf{N} = \mathbf{MK} \tag{4}$$

The master angular patterns $\{\boldsymbol{\theta}_j\}$ for the set of energetically favorable faces can be derived from eq 2. For example, the master angular patterns for two different polymorphs of acetaminophen are shown in Tables A1 and A2 of the Appendix. These angular patterns are unique for a given polymorph and are invariant with respect to morphologies of growing crystals.

Step 3. The experimental observation of crystal shape using confocal microscopy, described in section 3.2, can produce a matrix **N*** of normal vectors that can be further manipulated to obtain experimentally measured angular patterns $(\boldsymbol{\theta}_k^*)$

$$\theta_{l,k}^* = \cos^{-1}(n_l^* \cdot n_k^*), \qquad l, k = 1, 2, ..., m \tag{5}$$

where *m* is the number of experimentally observed crystal faces (for growing crystals $m \leq n$) and the asterisk (*) denotes that they are experimentally measured quantities. Although the Cartesian frames of reference for **N** and **N*** might not overlap, the angular patterns $\boldsymbol{\theta}_j$ and $\boldsymbol{\theta}_k^*$ (which are both arranged in ascending order) are independent of such differences. For example, the angular patterns computed for the experimentally measured normal vectors (Table A3, Appendix) are shown in Table A4 (Appendix).

Step 4. The experimentally measured angular patterns $\{\boldsymbol{\theta}_k^*\}_{k=1}^m$ can then be compared with the master angular patterns $\{\boldsymbol{\theta}_j\}_{j=1}^n$ of each polymorph. As the dimensions of $\boldsymbol{\theta}_k^*$ and $\boldsymbol{\theta}_j$ can be different, the match can be established under the condition that the set of components of $\boldsymbol{\theta}_k^*$ is a proper subset of the set of components of $\boldsymbol{\theta}_j$. The identification of the master angular patterns $\{\boldsymbol{\theta}_j\}_{j=1}^n$ that match with $\{\boldsymbol{\theta}_k^*\}_{k=1}^m$ would fix the polymorph of the crystal. For example, the match between Tables A4 and A1 confirms form I of acetaminophen crystals.

Step 5. Let $\boldsymbol{\nu}_1 = \mathbf{m}_j$ be the Miller index of *j*th face whose angular pattern $\boldsymbol{\theta}_j$ matches with some $\boldsymbol{\theta}_k^*$ with a normal vector of $\boldsymbol{\nu}_2 = \mathbf{n}_k^*$. The relation between the Cartesian frames of reference corresponding to **N** and **N*** can be obtained by using a rotation matrix as follows

$$\mathbf{n}_k^* = \mathbf{R}_\sigma \mathbf{n}_j = \mathbf{R}_\sigma \mathbf{K}^{\mathrm{T}} \mathbf{m}_j \tag{6}$$

The rotation matrix $\mathbf{R}_\sigma$ is given as

$$\mathbf{R}_\sigma = \begin{bmatrix} 1 & 0 & 0 \\ 0 & \cos\sigma_1 & \sin\sigma_1 \\ 0 & -\sin\sigma_1 & \cos\sigma_1 \end{bmatrix} \cdot \begin{bmatrix} \cos\sigma_2 & 0 & -\sin\sigma_2 \\ 0 & 1 & 0 \\ \sin\sigma_2 & 0 & \cos\sigma_2 \end{bmatrix} \cdot \begin{bmatrix} \cos\sigma_3 & \sin\sigma_3 & 0 \\ -\sin\sigma_3 & \cos\sigma_3 & 0 \\ 0 & 0 & 1 \end{bmatrix}$$

where σ_1, σ_2, and σ_3 are the counterclockwise rotations about the *x*, *y*, and *z* axes, respectively. The substitution of $\mathbf{m}_j = \boldsymbol{\nu}_1$ and $\mathbf{n}_k^* = \boldsymbol{\nu}_2$ in eq 6 would fix the rotational angles $\boldsymbol{\sigma} \equiv \{\sigma_1, \sigma_2, \sigma_3\}$ and, hence, the transformation matrix $(\mathbf{KR}_\sigma{}^{\mathrm{T}})$. Now, the Miller indices $(\mathbf{m}_k^*)$ of the experimentally measured normal vectors $(\mathbf{n}_k^*)$ can be directly obtained as

$$\mathbf{M}^* = \mathbf{N}^*(\mathbf{KR}_\sigma{}^{\mathrm{T}})^{-1} \tag{7}$$

Equation 7 identifies the crystallographic frame of reference from the experimentally measured crystal shape using the transformation matrix $(\mathbf{KR}_\sigma{}^{\mathrm{T}})$. The identification of the transformation matrix and the calculation of Miller indices for acetaminophen crystals are given in the Appendix. The information on the *h* vector and the corresponding Miller indices $(\mathbf{M}^*)$ can be further explored to study the polyhedral symmetry of the crystal to reduce the dimensions of the *h* vector. For example, a cubic crystal with identical faces will have repeating elements in the *h* vector measured with respect to the centroid of the crystal. Such considerations of symmetry are very important for reducing the dimensionality of dynamic models for shape evolution.[10]

3.4. Representation of Measurable Quantities Using the *h* Vector. There is a vast amount of literature on convex polyhedra calculations in the area of computational geometry. Simple programs for computing the surface areas, volumes, mean diameters, and so on of convex polyhedra are available in commercial software such as Matlab and Mathematica. The basis of such calculations lies in identifying the vertices of a convex polyhedron defined as $\mathbf{Nr} \leq \mathbf{h}$, where **r** is the position vector. The vertex of a polyhedron is formed by at least three faces that can be shown as

$$\mathbf{v} = [\mathbf{n}_i{}^{\mathrm{T}}\mathbf{n}_j{}^{\mathrm{T}}\mathbf{n}_k{}^{\mathrm{T}}]^{-1} \cdot \begin{bmatrix} h_i \\ h_j \\ h_k \end{bmatrix} \quad \text{such that} \quad |\mathbf{n}_i{}^{\mathrm{T}}\mathbf{n}_j{}^{\mathrm{T}}\mathbf{n}_k{}^{\mathrm{T}}| \neq 0$$

$$\text{and} \quad \mathbf{Nv} \leq \mathbf{h} \tag{8}$$

The set of vertices obtained for different combinations of crystal faces can be used to measure the face-specific area, total surface area, volume, and shape-related measures of the crystals.[8]

3.5. Image-Analysis Program. The image-analysis program consists of three modules that were developed using the image-processing toolbox of Matlab. The first module does image processing to obtain the contours of the crystals in the images, which might involve multiple treatments based on the quality of the image. As the quality of confocal images under fixed microscope operating conditions is relatively constant, the treatment to obtain contours is also fixed for a stack of confocal images. The images must be converted to grayscale and then subjected to contrast adjustment, if needed, using the Matlab

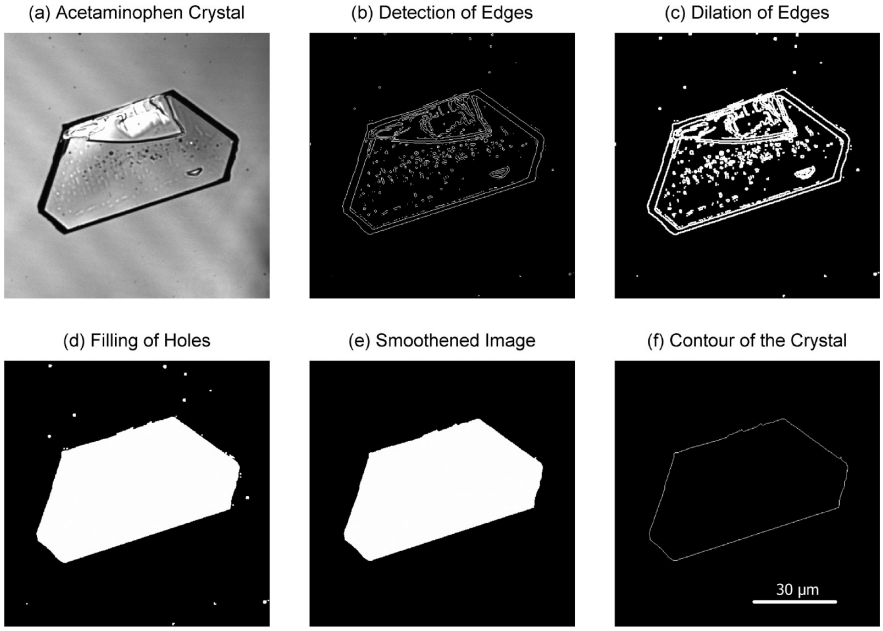

Figure 4. Image processing for segmenting crystals using Matlab: (a) CRM image of an acetaminophen crystal at 20× magnification, (b) binary mask generated using the Sobel method, (c) dilation of edges using linear structuring elements, (d) filling holes by a flood-filling operation, (e) smoothing the image by erosion, and (f) contour of the segmented image.

subroutine imadjust. The edges of the crystals in the images can then be found by using Matlab subroutine edge which is based on identifying intensity gradients in the intensity image. Finally, only those edges are selected that belongs to the contours of the crystals by filling holes and smoothing of the images. The image-processing treatments in this first module is very specific to the set of images obtained from a confocal microscope.

The second module collects the contours of different slices of a crystal in a given stack of confocal images with information on the distance between the slices. These contours are then fitted based on the methodology given in section 3.2 to yield the crystal shape (**h** and **N**).

The third module identifies the Miller indices of the crystal faces and hence the crystal polymorph. The detailed calculations for the identification of Miller indices (**M***) are presented in section 3.3. These three modules can be run for multiple confocal stacks to obtain morphology distributions with respect to *h* vectors.

4. MATERIALS AND METHODS

Crystals of acetaminophen of form I were grown by cooling a supersaturated solution of acetaminophen (MP Biomedicals, 90−100 wt %) in water at room temperature. There are many ways to produce acetaminophen crystals of form I, which will not be discussed here in detail because they can be found elsewhere.[53] The crystals were then filtered and dried, after which they were coated with a fluorescent dye. The basic requirement for 3D imaging using a confocal microscope is that the material should be fluorescent. Therefore, the coating of fluorescent dyes on crystals is important for the versatility of this technique. The instability of fluorescent molecules at high temperatures and their high molecular weights prevent their use for physical vapor deposition. Therefore, solution-based physical deposition was chosen to coat the fluorescent dye.

Most active pharmaceutical ingredients (APIs) are polar molecules with little or no solubility in nonpolar solvents. Lipophilic fluorescent molecules can be dissolved in some nonpolar solvents in which crystals of an API are suspended. The solution-based physical deposition of the fluorescent dye can be simply done by evaporating the nonpolar solvent. Acetaminophen crystals suspended in a solution of octadecyl rhodamine B chloride (R18, Invitrogen) in *n*-heptane were coated with the dye by evaporating the solvent. The coated crystals were taken on microscopic slides and observed by a confocal microscope (Bio-Rad MRC 1024) at an excitation wavelength of 568 nm and an emission filter at 605/32. The method can be extended to coat fluorescent dye on any material by choosing appropriate dye−solvent systems, hence enabling 3D imaging of the material using confocal microscopy.

5. RESULTS AND DISCUSSION

The performance of the morphology measurement techniques discussed in section 3 on the experimentally observed 2D and 3D shapes of acetaminophen is examined in the subsequent subsections. The image-analysis program was able to produce *h* vectors and Miller indices for different shapes of acetaminophen crystals and reliably generate morphology distributions for in silico images of 2D crystals.

5.1. Morphology of 2D Acetaminophen Crystals. Acetaminophen can take widely different shapes depending on the supersaturation regime. Platelike crystals of acetaminophen were synthesized at low supersaturation and observed by confocal reflection microscopy (CRM). As CRM relies on the detection of light reflected from a sample, it can be used to observe crystals without fluorescent tagging. CRM, however, suffers from blind spots that prevent the viewing of crystal faces at certain angles.[54] The image acquired by CRM was processed, as described in the first module of section 3.5, to obtain the contour of the crystal. Figure 4 shows the sequential treatments performed on the confocal micrograph to automatically segment the crystal. The binary mask (Figure 4b) of the image was created by detecting intensity gradients using the Sobel approximation. The thin high-contrast line in the binary mask was then dilated using flat linear structuring elements (Figure 4c). The holes in the dilated image were filled using the flood-fill operation on the background pixels. Figure 4d was further smoothed by eroding the image using diamond-shaped structuring elements. The segmented crystal can be clearly seen in Figure 4e, and its contour (Figure 4d) was easily identified by picking the boundary pixels. Although this set of operations was specific for

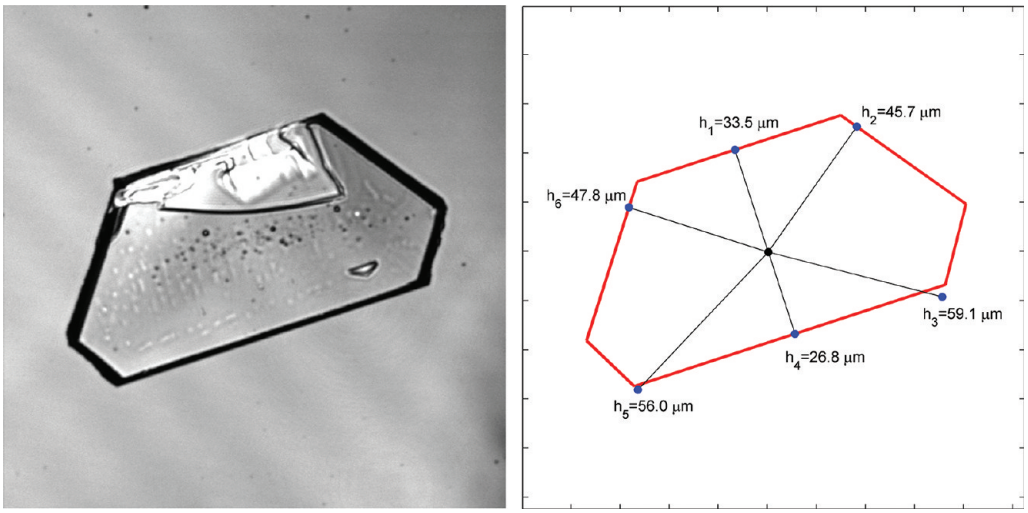

Figure 5. Identification of the polygon that best fits the crystal shape.

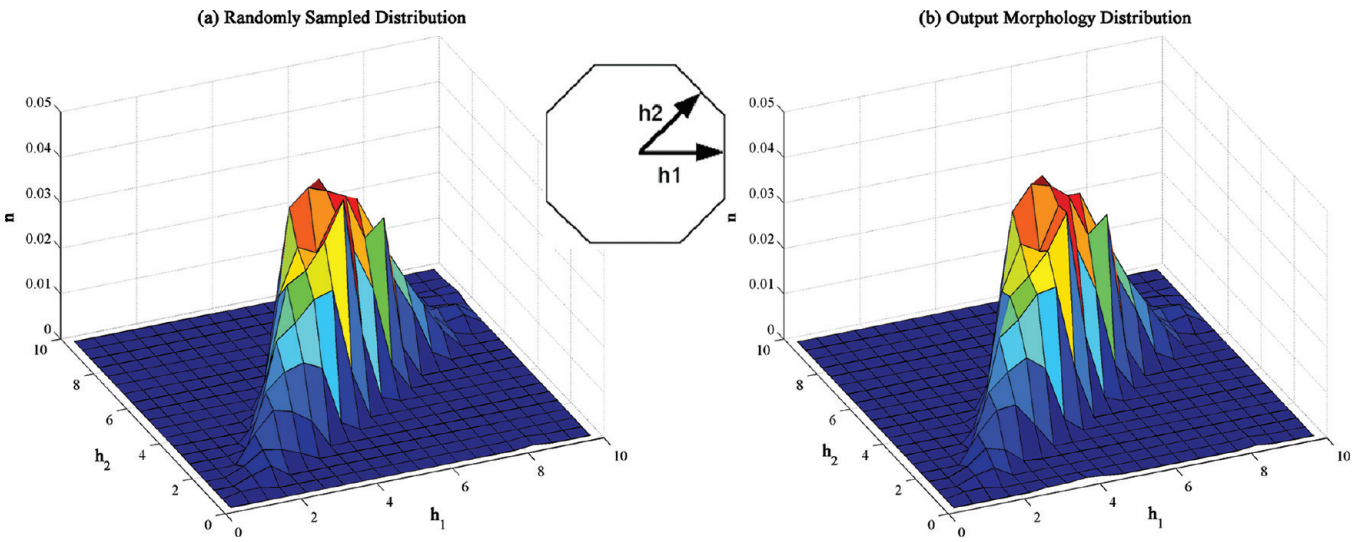

Figure 6. Measured morphology distribution of octagonal crystals: (a) randomly sampled points from bivariate Gaussian distribution and images of octagonal crystals created for each sampled point and (b) morphology distribution obtained after analyzing images of octagonal crystals.

this image, the operations can be easily automated for other images obtained by confocal microscopy under similar conditions.

The contour obtained from image processing was analyzed to identify the crystal facets. The methodology described in section 3.1 groups the pixels lying on the flat elements by drawing a convex hull. The pixels nearest the face of the convex hull can be easily identified to form a group that also represents a crystal face. The number of facets in the convex hull might exceed the number of crystal faces, leading to more than one group for the same crystal face. Each group of pixels was subjected to linear regression to obtain the normal vectors ($\mathbf{n}_k^*$) and perpendicular distances (h vector). Clearly, if two groups correspond to the same crystal face, then their normal vectors and h vectors will also be the same, resulting in the rapid identification of the unique crystal faces.

The final form of the polygon that fits well to the projected image of crystal is shown in Figure 5 (right). This analysis identified six crystal faces ordered in counterclockwise direction with their perpendicular distances from the center. The equilibrium morphology of acetaminophen crystals grown at low supersaturation has four families of energetically favorable faces, namely, {110}, {001}, {201}, and {011}.[51] Comparison of the crystal shape in Figure 5 with its equilibrium morphology indicates that {110} comprises the top, bottom, first, and fourth faces; {001} represents inclined faces whose projections form the third and sixth faces; and finally, {201} and {011} are projected along the second and fifth faces. In this case, the identification of Miller indices requires that angular patterns be measured in the plane of projection and matched with the master angular patterns. The current analysis on 2D crystals can be applied to a wide class of materials such as succinic acid and gibbsite where the effect of inclined planes on the h vector is not significant. The next subsections describe the capabilities of the image-analysis program to perform repeated measurements to yield morphology distributions.

5.2. Morphology Distributions of 2D Crystals. The images of 2D crystals are easy to capture and process using the methodology described in section 5.1. To test this image-analysis program, we generated and analyzed 10000 images of octagonal crystals with two characteristic dimensions corresponding to two families of faces forming squares and

diamonds. The generation of images involves the random selection of 10000 points from a known bivariate Gaussian distribution (see Figure 6a) and the creation of images of octagonal crystals in Matlab for each randomly selected point. These 10000 images were stored in a computer so that the image-analysis program could access them automatically. These images were sequentially analyzed by the image-analysis program to obtain the bivariate distribution of their characteristic lengths (h_1 and h_2).

The purpose of this part of the study was to check the amount of error induced by the image-analysis program in the measurement of morphology distributions. Figure 6 shows that there was a close match between the sampled distribution and the measured distribution, with a relative error on the order of 10^{-3}. Although the error was not significant, a possible source could be the fitting of polygons to the crystal images.

5.3. Morphology of 3D Crystals. The necessity for determining three-dimensional shapes of crystals in many applications calls for robust and reliable tomographic techniques to measure them. Confocal microscopy provides much simpler settings for acquiring tomographic images than X-ray microscopy. The acquisition of better images involves not only the proper sample-preparation techniques but also the optimum choice of factors such as $x-y$ resolution, number of slices, diameter of pinhole aperture, gain, and offset. A tradeoff is often made between the optimum resolution and the time required for imaging. There are a few applications of the automation of confocal microscopes, including online monitoring of particle deposition on a membrane,[12,13] which suggests the possibility of online measurements of crystal shapes.

Fluorescent-dye-coated acetaminophen crystals were observed with a confocal microscope at 10× magnification. The two projected images of acetaminophen crystals are shown in Figure 7. These projected images were constructed by combining all confocal slices to get in-depth resolution. It can be seen that the quality of the images is greatly affected by the nonuniform coating of fluorescent dye, which calls for more advanced coating technologies. The crystals shown in Figure 7 are on the order of 100 μm and can be viewed in air medium at lower magnification; however, crystals in the micrometer and submicrometer range requiring higher magnification might need oil medium to obtain proper contrast, which can cause bleeding of the fluorescent dye during microscopy. The quick imaging of such bleeding crystals is the simplest remedy for this problem.

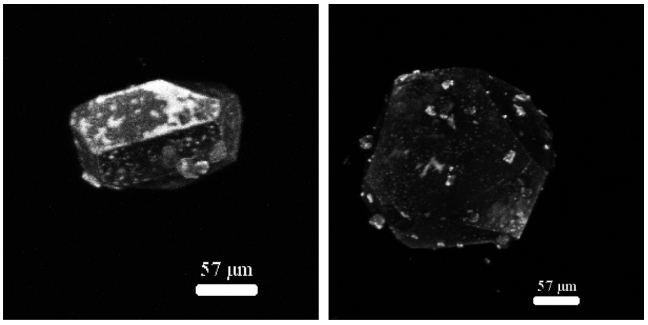

Figure 7. Confocal images of acetaminophen crystals coated with octadecyl rhodamine B chloride.

The 29 confocal slices of the crystal shown in Figure 7 (left) were processed in a fashion similar to that used for Figure 4 to obtain contours for the set of slices. These contours were then analyzed, as described in section 3.2, to obtain the polyhedron that best fits the crystal (see Figure 8). The resolution of the polyhedron strongly depends on the number of slices considered for regression, which can affect the time efficiency of examining a population of crystals.

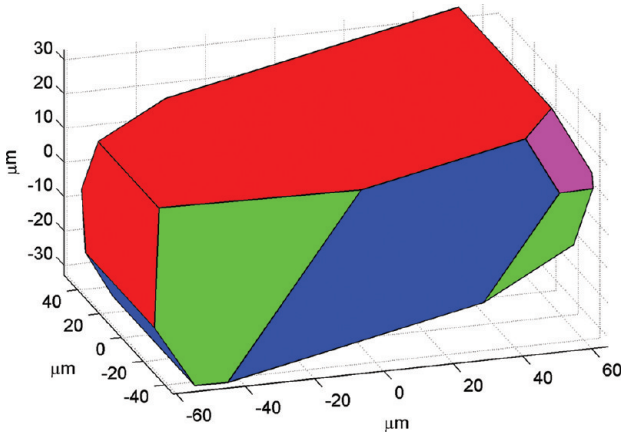

Figure 8. Identification of the polyhedron that best fits the tomographic images of the acetaminophen crystal shown in Figure 7 (left).

The two basic outcomes of the image-analysis program include normal vectors and the h vector, which can be used to measure all other shape-related properties, as discussed in section 3.4, such as face-specific area, total surface area, volume, sphericity, and equivalent diameters. Some results for the crystals in Figure 8 are shown in Table 2, including the Miller indices of the faces, their perpendicular distances, and their face-specific areas. The other calculated quantities of the crystal, for example, are total area (39436.29 μm^2), volume (492040 μm^3), sphericity (0.7643), and Sauter mean diameter (74.86 μm).

Table 2. Miller Indices, h Vectors, and Face-Specific Areas of the Crystal in Figure 8

Miller index	h (μm)	area (μm^2)
$(1\bar{1}0)$	21.53	10050.20
$(\bar{1}10)$	21.53	10991.11
$(\bar{1}\bar{1}0)$	56.53	1943.14
(110)	61.53	1757.64
(011)	67.10	314.75
$(01\bar{1})$	57.10	714.29
$(0\bar{1}\bar{1})$	47.10	1875.75
$(0\bar{1}1)$	62.10	425.30
(001)	52.38	4268.19
$(00\bar{1})$	47.38	2993.87
(100)	62.38	1976.29
$(\bar{1}00)$	62.38	1065.10
$(\bar{2}01)$	69.11	617.54
$(20\bar{1})$	69.11	443.14

These normal vectors were used to generate angular patterns that were then matched with the master angular patterns to identify the polymorph. The details of these calculations are presented in the Appendix, which confirms that the crystal in Figure 8 is of form I.

6. CONCLUSIONS

The purpose of this article has been (i) to review existing technologies for measuring crystal morphologies, (ii) to introduce the application of confocal microscopy as a promising technique for obtaining tomographic images of crystals, and (iii) to show how tomographic images can be utilized to obtain quantitative crystal morphology defined by the *h* vector that can also generate all other shape descriptors. We have addressed here three different issues related to image acquisition, image processing, and image analysis. The novelty of this work lies in the acquisition of tomographic images of crystals using confocal microscopy and analysis of tomographic images to obtain crystal shapes (in terms of the *h* vector and normal vectors) and identify polymorphs and Miller indices of the faces.

Tomographic techniques are by far the most accurate ones for measuring 3D shapes, and of these, confocal microscopy definitely has some advantages over other techniques. Some of these advantages are as follows:

(1) The sample requirements are not as stringent as with X-ray tomography. The only requirement is the identification of a suitable fluorescent dye that can coat crystals. As most pharmaceutical crystals are made up of polar molecules, they can be coated with lipophilic dyes such as octadecyl rhodamine B chloride that are soluble in the solvents such as heptane.

(2) The sample must be crystalline to observe under X-ray microscope, whereas there are no such requirements for confocal microscopy, except that the material must be uniformly coated with a suitable fluorescent dye.

(3) The resolution of confocal microscopes can be as small as 190 nm, which is much smaller than the resolution of X-ray microscopes.

(4) Image acquisition using confocal microscopes is faster than that with X-ray microscopes.

These advantages make the confocal microscope a versatile instrument for measuring 3D shapes of crystalline or amorphous materials provided the sources of uncertainties are identified. Some issues relating to improvements in the capabilities of the confocal microscope are (1) automated provision for the optimization of operating conditions of confocal microscopes specific to fluorescent-dye-coated crystals with respect to adjustments for pinhole aperture, gain, offset, and $x-y-z$ resolutions and (2) improved coating procedures for fluorescent dye to identify slices with suitable image-processing tools.

Opportunities abound for the application of confocal microscopy in particle technology, in situations where (1) a fluorescent dye can be coated uniformly onto the crystal and (2) the tomographic images can be analyzed for its shape and polymorph. This article presents a simple way to obtain crystal morphology from

Table A1. Angular Patterns for Form I with Lattice Parameters a = 12.651 Å, b = 8.887 Å, c = 7.236 Å, $\alpha = \beta$ = 90°, γ = 114.848°

	$\mathbf{m}_j$													
no.	$(00\bar{1})$	$(\bar{1}00)$	(001)	(100)	$(01\bar{1})$	$(0\bar{1}1)$	(011)	$(0\bar{1}\bar{1})$	$(20\bar{1})$	$(\bar{2}01)$	(110)	$(\bar{1}10)$	$(1\bar{1}0)$	$(\bar{1}\bar{1}0)$
1	0.00	0.00	0.00	0.00	0.00	0.00	0.00	0.00	0.00	0.00	0.00	0.00	0.00	0.00
2	41.90	38.42	41.90	38.42	41.90	41.90	41.90	41.90	38.42	38.42	38.95	60.31	60.31	38.95
3	41.90	38.95	41.90	38.95	46.97	46.97	53.19	53.19	46.97	46.97	52.46	60.31	60.31	52.46
4	51.58	72.72	51.58	72.72	53.19	53.19	60.31	60.31	51.58	51.58	53.19	68.33	68.33	53.19
5	90.00	73.70	90.00	73.70	60.31	60.31	73.70	73.70	52.46	52.46	53.19	72.72	72.72	53.19
6	90.00	73.70	90.00	73.70	73.70	73.70	75.95	75.95	75.95	75.95	68.33	76.54	76.54	68.33
7	90.00	90.00	90.00	90.00	83.80	83.80	83.80	83.80	76.54	76.54	90.00	90.00	90.00	90.00
8	90.00	90.00	90.00	90.00	96.20	96.20	96.20	96.20	103.46	103.46	90.00	90.00	90.00	90.00
9	90.00	106.30	90.00	106.30	106.30	106.30	104.05	104.05	104.05	104.05	111.67	103.46	103.46	111.67
10	90.00	106.30	90.00	106.30	119.69	119.69	106.30	106.30	127.54	127.54	126.81	107.28	107.28	126.81
11	128.42	107.28	128.42	107.28	126.81	126.81	119.69	119.69	128.42	128.42	126.81	111.67	111.67	126.81
12	138.10	141.05	138.10	141.05	133.03	133.03	126.81	126.81	133.03	133.03	127.54	119.69	119.69	127.54
13	138.10	141.58	138.10	141.58	138.10	138.10	138.10	138.10	141.58	141.58	141.05	119.69	119.69	141.05
14	180.00	180.00	180.00	180.00	180.00	180.00	180.00	180.00	180.00	180.00	180.00	180.00	180.00	180.00

Table A2. Angular Patterns for Form II with Lattice Parameters a = 7.308 Å, b = 11.804 Å, c = 17.161 Å, $\alpha = \beta$ = 90°

	$\mathbf{m}_j$													
no.	$(00\bar{1})$	$(\bar{1}00)$	(001)	(100)	$(01\bar{1})$	$(0\bar{1}1)$	(011)	$(0\bar{1}\bar{1})$	$(20\bar{1})$	$(\bar{2}01)$	(110)	$(\bar{1}10)$	$(1\bar{1}0)$	$(\bar{1}\bar{1}0)$
1	0.00	0.00	0.00	0.00	0.00	0.00	0.00	0.00	0.00	0.00	0.00	0.00	0.00	0.00
2	55.48	12.02	55.48	12.02	55.48	55.48	55.48	55.48	12.02	12.02	31.76	31.76	31.76	31.76
3	55.48	31.76	55.48	31.76	64.30	64.30	64.30	64.30	33.74	33.74	33.74	33.74	33.74	33.74
4	77.98	31.76	77.98	31.76	64.30	64.30	64.30	64.30	33.74	33.74	63.53	63.53	63.53	63.53
5	90.00	90.00	90.00	90.00	69.04	69.04	69.04	69.04	77.98	77.98	64.30	64.30	64.30	64.30
6	90.00	90.00	90.00	90.00	83.22	83.22	83.22	83.22	83.22	83.22	64.30	64.30	64.30	64.30
7	90.00	90.00	90.00	90.00	90.00	90.00	90.00	90.00	83.22	83.22	90.00	90.00	90.00	90.00
8	90.00	90.00	90.00	90.00	90.00	90.00	90.00	90.00	96.78	96.78	90.00	90.00	90.00	90.00
9	90.00	90.00	90.00	90.00	96.78	96.78	96.78	96.78	96.78	96.78	115.70	115.70	115.70	115.70
10	90.00	90.00	90.00	90.00	110.96	110.96	110.96	110.96	102.02	102.02	115.70	115.70	115.70	115.70
11	102.02	148.24	102.02	148.24	115.70	115.70	115.70	115.70	146.26	146.26	116.47	116.47	116.47	116.47
12	124.52	148.24	124.52	148.24	115.70	115.70	115.70	115.70	146.26	146.26	146.26	146.26	146.26	146.26
13	124.52	167.98	124.52	167.98	124.52	124.52	124.52	124.52	167.98	167.98	148.24	148.24	148.24	148.24
14	180.00	180.00	180.00	180.00	180.00	180.00	180.00	180.00	180.00	180.00	180.00	180.00	180.00	180.00

tomographic images using a convex hull. The convex hull facilitates the identification of crystal faces and is followed by a regression procedure to obtain surface normals and the h vector. The identification of master angular patterns readily allows for the detection of polymorphs.

The current methodology for obtaining the h vector for 2D crystals can also be used with other projection-based techniques such as PVM and optical microscopy. The analysis of 2D crystals can reliably produce h vectors and normal vectors if the inclination of the planes with respect to the projection plane is known. The methodology for measuring 3D shapes from tomographic images can also be extended to stereoscopic images. The dynamic 3D images of crystals can also be obtained from hot-stage confocal microscopes if there are provisions for intermittent coating and removal of fluorescent dyes.

As demonstrated, quick assessment of the morphology of single crystals allows for the determination of the morphology distribution among a population of crystals. However, for the determination of morphology distributions, it is essential to develop the capability for online measurements. In this regard, the work of Patience and Rawlings[27] is particularly noteworthy for emulation. Alternatively, confocal microscopy can also be used for the offline imaging of crystals sampled frequently from crystallizers. What this work has accomplished is a methodology for the rapid assessment of the morphologies of faceted objects when their images are available.

Table A3. Normal Vectors Derived from Crystal Shape Measurements in Figure 8

$\mathbf{n}_1^*$	0.0000	0.0000	1.0000
$\mathbf{n}_2^*$	−0.9307	0.0000	0.3659
$\mathbf{n}_3^*$	0.4427	−0.7478	−0.4948
$\mathbf{n}_4^*$	0.4427	0.7478	−0.4948
$\mathbf{n}_5^*$	0.0000	1.0000	0.0000
$\mathbf{n}_6^*$	0.0000	−1.0000	0.0000
$\mathbf{n}_7^*$	−0.4427	−0.7478	0.4948
$\mathbf{n}_8^*$	0.0000	0.0000	−1.0000
$\mathbf{n}_9^*$	0.9493	0.0000	0.3144
$\mathbf{n}_{10}^*$	0.7407	−0.6255	0.2453
$\mathbf{n}_{11}^*$	−0.4427	0.7478	0.4948
$\mathbf{n}_{12}^*$	−0.7407	0.6255	−0.2453
$\mathbf{n}_{13}^*$	0.9307	0.0000	−0.3659
$\mathbf{n}_{14}^*$	−0.9493	0.0000	−0.3144

APPENDIX

Miller Index and Polymorph Identification

Acetaminophen crystals are known to exist in three polymorphic forms: form I (monoclinic, stable), form II (orthorhombic, metastable), and form III (Unknown). These polymorphs of acetaminophen have four energetically favorable families of faces (F faces), namely, {110}, {001}, {201}, and {011}, that form a tetradecahedron. The master angular patterns for forms I and II were generated using eq 2 and are listed in Tables A1 and A2, respectively.

The normal vectors of the crystal faces obtained from the shape measurements are given in Table A3. The objective of this analysis was to identify the polymorph of the crystal and the Miller indices corresponding to the normal vectors. The angular patterns (shown in Table A4) obtained from the measured normal vectors matches significantly with Table A1, which confirms its polymorph to be form I. The assignment of the Miller indices requires the identification of the transformation matrix ($\mathbf{KR}_\sigma^{\mathrm{T}}$). We use eq 6 to find the rotations about the axes for some pairs ($\mathbf{n}_k^*$, $\mathbf{m}_j$) that correspond to the columns of Tables A4 and A1 with similar angular patterns. We need two pairs of ($\mathbf{n}_k^*$, $\mathbf{m}_j$) to uniquely determine the angular rotations. The two arbitrary choices of pairs ($\mathbf{n}_1^*$, $\mathbf{m}_{13}$) and ($\mathbf{n}_6^*$, $\mathbf{m}_1$) yielded angular rotations $\boldsymbol{\sigma} = [90°\ 0°\ 18.324°]$ using eq 6. The knowledge of lattice parameters and angular rotations fixes the transformation matrix, which in Table A3 directly produces the corresponding Miller indices, as shown in Table A5.

Table A5. Identified Miller Indices for Crystal Faces

$\mathbf{m}_1^*$	1.00	−1.00	0.00
$\mathbf{m}_2^*$	−1.00	−1.00	0.00
$\mathbf{m}_3^*$	0.00	1.00	−1.00
$\mathbf{m}_4^*$	0.00	1.00	1.00
$\mathbf{m}_5^*$	0.00	0.00	1.00
$\mathbf{m}_6^*$	0.00	0.00	−1.00
$\mathbf{m}_7^*$	0.00	−1.00	−1.00
$\mathbf{m}_8^*$	−1.00	1.00	0.00
$\mathbf{m}_9^*$	1.00	0.00	0.00
$\mathbf{m}_{10}^*$	2.00	0.00	−1.00
$\mathbf{m}_{11}^*$	0.00	−1.00	1.00
$\mathbf{m}_{12}^*$	−2.00	0.00	1.00
$\mathbf{m}_{13}^*$	1.00	1.00	0.00
$\mathbf{m}_{14}^*$	−1.00	0.00	0.00

Table A4. Angular Patterns Corresponding to the Normal Vectors Given in Table A3

	$\mathbf{n}_k^*$													
no.	$\mathbf{n}_1^*$	$\mathbf{n}_2^*$	$\mathbf{n}_3^*$	$\mathbf{n}_4^*$	$\mathbf{n}_5^*$	$\mathbf{n}_6^*$	$\mathbf{n}_7^*$	$\mathbf{n}_8^*$	$\mathbf{n}_9^*$	$\mathbf{n}_{10}^*$	$\mathbf{n}_{11}^*$	$\mathbf{n}_{12}^*$	$\mathbf{n}_{13}^*$	$\mathbf{n}_{14}^*$
1	0.00	0.00	0.00	0.00	0.00	0.00	0.00	0.00	0.00	0.00	0.00	0.00	0.00	0.00
2	60.35	39.79	41.60	41.60	41.60	41.60	41.60	60.35	38.72	38.72	41.60	38.72	39.79	38.72
3	60.35	53.16	47.60	53.62	41.60	41.60	53.62	60.35	39.79	47.60	47.60	47.60	53.16	39.79
4	68.54	53.62	53.62	60.35	51.28	51.28	60.35	68.54	71.68	51.28	53.62	51.28	53.62	71.68
5	71.68	53.62	60.35	74.65	90.00	90.00	74.65	71.68	74.65	53.16	60.35	53.16	53.62	74.65
6	75.80	68.54	74.65	74.86	90.00	90.00	74.86	75.80	74.65	74.86	74.65	74.86	68.54	74.65
7	90.00	90.00	83.20	83.20	90.00	90.00	83.20	90.00	90.00	75.80	83.20	75.80	90.00	90.00
8	90.00	90.00	96.80	96.80	90.00	90.00	96.80	90.00	90.00	104.20	96.80	104.20	90.00	90.00
9	104.20	111.46	105.35	105.14	90.00	90.00	105.14	104.20	105.35	105.14	105.35	105.14	111.46	105.35
10	108.32	126.38	119.65	105.35	90.00	90.00	105.35	108.32	105.35	126.84	119.65	126.84	126.38	105.35
11	111.46	126.38	126.38	119.65	128.72	128.72	119.65	111.46	108.32	128.72	126.38	128.72	126.38	108.32
12	119.65	126.84	132.40	126.38	138.40	138.40	126.38	119.65	140.21	132.40	132.40	132.40	126.84	140.21
13	119.65	140.21	138.40	138.40	138.40	138.40	138.40	119.65	141.28	141.28	138.40	141.28	140.21	141.28
14	180.00	180.00	180.00	180.00	180.00	180.00	180.00	180.00	180.00	180.00	180.00	180.00	180.00	180.00

AUTHOR INFORMATION

Corresponding Author
*E-mail: ramkrish@ecn.purdue.edu.

Notes
The authors declare no competing financial interest.

ACKNOWLEDGMENTS

M.R.S. and D.R. gratefully acknowledge current and past funding support from Abbott Laboratories, Roche Pharmaceuticals, and the NSF Engineering Research Center for Structured Organic Particulate Systems for this research. We are thankful to Dr. Ram Narayan (Roche Carolina) for useful discussions on morphology measurements, Dr. Steef X. M. Boerrigter (SSCI/Aptuit) for providing suggestions on polymorph identification, Prof. Alexander Wei (Chemistry, Purdue) for providing access to CRM, Dr. Gerard Gagne for suggesting fluorescent dyes and providing access to the confocal microscope facility at Abbott Park. M.R.S. and D.R. are also grateful to GPRD-Process Engineering Department of Abbott Laboratories for providing the opportunity to conduct part of this research at its facilities.

REFERENCES

(1) Schwarcz, H.; Shane, K. Measurement of particle shape by Fourier analysis. *Sedimentology* **1969**, *13* (3−4), 213−231. Luerkens, D.; Beddow, J.; Vetter, A. Morphological Fourier descriptors. *Powder Technol.* **1982**, *31* (2), 209−215.

(2) Clark, N. Three techniques for implementing digital fractal analysis of particle shape. *Powder Technol.* **1986**, *46* (1), 45−52.

(3) Hütter, M.; Rutledge, G.; Armstrong, R. Crystal shapes and crystallization in continuum modeling. *Phys. Fluids* **2005**, *17*, 014107.

(4) Mokhtarian, F.; Mackworth, A. A theory of multiscale, curvature-based shape representation for planar curves. *IEEE Trans. Pattern Anal. Mach. Intell.* **1992**, 789−805.

(5) Keren, D.; Cooper, D.; Subrahmonia, J. Describing complicated objects by implicit polynomials. *IEEE Trans. Pattern Anal. Mach. Intell.* **1994**, 38−53. Carr, J.; Beatson, R.; Cherrie, J.; Mitchell, T.; Fright, W.; McCallum, B.; Evans, T. Reconstruction and Representation of 3D Objects with Radial Basis Functions. In *SIGGRAPH '01: Proceedings of the 28th Annual Conference on Computer Graphics and Interactive Techniques* ; ACM: New York, 2001; pp 67−76.

(6) Loncaric, S. A survey of shape analysis techniques. *Pattern Recognit.* **1998**, *31* (8), 983−1001. da Fontoura Costa, L.; Cesar, R. *Shape Analysis and Classification: Theory and Practice*; CRC Press: Boca Raton, FL, 2001.

(7) Zhang, Y.; Doherty, M. Simultaneous prediction of crystal shape and size for solution crystallization. *AIChE J.* **2004**, *50* (9), 2101−2112. Wan, J.; Wang, X.; Ma, C. Particle shape manipulation and optimization in cooling crystallization involving multiple crystal morphological forms. *AIChE J.* **2009**, *55* (8), 2049−2061.

(8) Borchert, C.; Nere, N.; Ramkrishna, D.; Voigt, A.; Sundmacher, K. On the prediction of crystal shape distributions in a steady-state continuous crystallizer. *Chem. Eng. Sci.* **2009**, *64* (4), 686−696.

(9) Ma, D.; Tafti, D.; Braatz, R. High-resolution simulation of multidimensional crystal growth. *Ind. Eng. Chem. Res.* **2002**, *41* (25), 6217−6223. Chakraborty, J.; Kumar, S. A new framework for solution of multidimensional population balance equations. *Chem. Eng. Sci.* **2007**, *62* (15), 4112−4125.

(10) Chakraborty, J.; Singh, M. R.; Ramkrishna, D.; Borchert, C.; Sundmacher, K. Modeling of crystal morphology distributions. Towards crystals with preferred asymmetry. *Chem. Eng. Sci.* **2010**, *65* (21), 5676−5686.

(11) Kelderman, H. F.; Fein, M. E.; Loh, A. E.; Adams, A.; Neukermans, A. P. (Tencor Instruments). Confocal measuring microscope with automatic focusing. U.S. Patent 4,844,617, 1989.

(12) Ferrando, M.; Zator, M.; López, F.; Güell, C. Confocal Scanning Laser Microscopy: Fundamentals and Uses on Membrane Fouling Characterization and Opportunities for Online Monitoring. In *Monitoring and Visualizing Membrane-Based Processes*, Güell, C., Ferrando, M., López, F., Eds.; Wiley-VCH: Weinheim, Germany, 2009; pp 55−75.

(13) Kromkamp, J.; Faber, F.; Schroen, K.; Boom, R. Effects of particle size segregation on crossflow microfiltration performance: Control mechanism for concentration polarisation and particle fractionation. *J. Membr. Sci.* **2006**, *268* (2), 189−197.

(14) Vorburger, T.; Teague, E. Optical techniques for on-line measurement of surface topography. *Precis. Eng.* **1981**, *3* (2), 61−83.

(15) Adrian, R. Particle-imaging techniques for experimental fluid mechanics. *Annu. Rev. Fluid Mech.* **1991**, *23* (1), 261−304.

(16) Chen, F.; Brown, G.; Song, M. Overview of three-dimensional shape measurement using optical methods. *Opt. Eng.* **2000**, *39* (1), 10−22.

(17) Viswanathan, K.; Aravamudhan, S.; Mani, B. Separation Based on Shape Part I: Recovery Efficiency of Spherical Particles. *Powder Technol.* **1984**, *39* (1), 83−91.

(18) Nakagawa, M.; Furuuchi, M.; Yamahata, M.; Gotoh, K.; Beddow, J. Shape classification of granular materials by rotating cylinder with blades. *Powder Technol.* **1985**, *44* (2), 195−202.

(19) Meloy, T.; Clark, N.; Durney, T.; Pitchumani, B. Measuring the particle shape mix in a powder with the cascadograph. *Chem. Eng. Sci.* **1985**, *40* (7), 1077−1084.

(20) Ma, Z.; Merkus, H.; de Smet, J.; Heffels, C.; Scarlett, B. New developments in particle characterization by laser diffraction: Size and shape. *Powder Technol.* **2000**, *111* (1−2), 66−78.

(21) Nere, N.; Ramkrishna, D.; Parker, B.; Bell, W., III; Mohan, P. Transformation of the Chord-Length Distributions to Size Distributions for Nonspherical Particles with Orientation Bias. *Ind. Eng. Chem. Res.* **2007**, *46* (10), 3041−3047.

(22) Paschotta, R. *Encyclopedia of Laser Physics and Technology*; Wiley-VCH: Weinheim, Germany, 2008.

(23) Singer, H. Measurements of the three-dimensional shape of ice crystals in supercooled water. *Phys. Rev. E* **2006**, *73* (5), 51606.

(24) Robinson, I.; Vartanyants, I.; Williams, G.; Pfeifer, M.; Pitney, J. Reconstruction of the shapes of gold nanocrystals using coherent x-ray diffraction. *Phys. Rev. Lett.* **2001**, *87* (19), 195505.

(25) Prasad, A. Stereoscopic particle image velocimetry. *Exp. Fluids* **2000**, *29* (2), 103−116.

(26) Bujak, B.; Bottlinger, M. Three-Dimensional Measurement of Particle Shape. *Part. Part. Syst. Charact.* **2008**, *25* (4), 293−297.

(27) Patience, D.; Rawlings, J. Particle shape monitoring and control in crystallization processes. *AIChE J.* **2001**, *47* (9), 2125−2130.

(28) Webb, R. Confocal optical microscopy. *Rep. Prog. Phys.* **1996**, *59*, 427−471.

(29) Larson, B.; Yang, W.; Ice, G.; Budai, J.; Tischler, J. Three-dimensional X-ray structural microscopy with submicrometre resolution. *Nature* **2002**, *415* (6874), 887−890.

(30) Patchigolla, K.; Wilkinson, D. Crystal Shape Characterisation of Dry Samples Using Microscopic and Dynamic Image Analysis. *Part. Part. Syst. Charact.* **2009**, *26* (4), 171−178.

(31) Chang, S.; Shih, C.; Chen, C.; Lai, W.; Wang, C. The shape transition of gold nanorods. *Langmuir* **1999**, *15* (3), 701−709.

(32) Braatz, R.; Hasebe, S. Particle Size and Shape Control in Crystallization Processes. *AIChE Symp. Ser.* **1998**, *326*, 307−327.

(33) Hansma, P.; Elings, V.; Marti, O.; Bracker, C. Scanning tunneling microscopy and atomic force microscopy: Application to biology and technology. *Science* **1988**, *242* (4876), 209−216.

(34) Myshkin, N.; Grigoriev, A.; Kholodilov, O. Quantitative analysis of surface topography using scanning electron microscopy. *Wear* **1992**, *153* (1), 119−133.

(35) Hentschel, M.; Page, N. Selection of descriptors for particle shape characterization. *Part. Part. Syst. Charact.* **2003**, *20* (1), 25−38.

(36) Pons, M.; Vivier, H.; Belaroui, K.; Bernard-Michel, B.; Cordier, F.; Oulhana, D.; Dodds, J. Particle morphology: From visualisation to measurement. *Powder Technol.* **1999**, *103* (1), 44−57.

(37) Podczeck, F.; Rahman, S.; Newton, J. Evaluation of a standardised procedure to assess the shape of pellets using image analysis. *Int. J. Pharm.* **1999**, *192* (2), 123−138.
(38) Wang, X.; Roberts, K.; Ma, C. Crystal growth measurement using 2D and 3D imaging and the perspectives for shape control. *Chem. Eng. Sci.* **2008**, *63* (5), 1173−1184.
(39) Simon, L.; Merz, T.; Dubuis, S.; Lieb, A.; Hungerbuhler, K. In-situ monitoring of pharmaceutical and specialty chemicals crystallization processes using endoscopy−stroboscopy and multivariate image analysis. *Chem. Eng. Res. Des.*, published online Apr 5, 2012, http://dx.doi.org/10.1016/j.cherd.2012.03.023.
(40) Wang, X.; Calderon De Anda, J.; Roberts, K.; Li, R.; Thomson, G.; White, G. Advances in on-line monitoring and control of the morphological and polymorphic forms of organic crystals grown from solution. *Kona* **2005**, *23*, 69−85.
(41) Kempkes, M.; Vetter, T.; Mazzotti, M. Measurement of 3D particle size distributions by stereoscopic imaging. *Chem. Eng. Sci.* **2010**, *65* (4), 1362−1373.
(42) Tiziani, H.; Uhde, H. Three-dimensional image sensing by chromatic confocal microscopy. *Appl. Opt.* **1994**, *33* (10), 1838−1843.
(43) Kindratenko, V. Development and application of image analysis techniques for identification and classification of microscopic particles. Ph.D. Thesis, Universitaire Antwerpen, Antwerp, Belgium, 1997.
(44) Bharati, M.; MacGregor, J. Multivariate image analysis for real-time process monitoring and control. *Ind. Eng. Chem. Res.* **1998**, *37* (12), 4715−4724. Sarkar, D.; Doan, X.; Ying, Z.; Srinivasan, R. In situ particle size estimation for crystallization processes by multivariate image analysis. *Chem. Eng. Sci.* **2009**, *64* (1), 9−19.
(45) Li, R.; Thomson, G.; White, G.; Wang, X.; De Anda, J.; Roberts, K. Integration of crystal morphology modeling and on line shape measurement. *AIChE J.* **2006**, *52* (6), 2297−2305.
(46) Larsen, P.; Rawlings, J.; Ferrier, N. Model-based object recognition to measure crystal size and shape distributions from in situ video images. *Chem. Eng. Sci.* **2007**, *62* (5), 1430−1441.
(47) Burns, J. B.; Hanson, A. R.; Riseman, E. M. Extracting straight lines. *IEEE Trans. Pattern Anal. Mach. Intell.* **1986**, *8* (4), 425−455.
(48) Barber, C. B.; Dobkin, D. P.; Huhdanpaa, H. The quickhull algorithm for convex hulls. *ACM Trans. Math. Software* **1996**, *22* (4), 469−483.
(49) Green, D.; Meenan, P.; Sunshine, G.; Ennis, B. Habit modelling and verification for glutaric acid. *J. Phys. D: Appl. Phys.* **1993**, *26*, B35−B40.
(50) Boerrigter, S.; Cuppen, H.; Ristic, R.; Sherwood, J.; Bennema, P.; Meekes, H. Explanation for the supersaturation-dependent morphology of monoclinic paracetamol. *Cryst. Growth Des.* **2002**, *2* (5), 357−361.
(51) Ristic, R.; Finnie, S.; Sheen, D.; Sherwood, J. Macro- and micromorphology of monoclinic paracetamol grown from pure aqueous solution. *J. Phys. Chem. B* **2001**, *105* (38), 9057−9066.
(52) Bond, W. Computation of interfacial angles, interzonal angles, and clinographic projection by matrix methods. *Am. Mineral.* **1946**, *31*, 31−42.
(53) Nichols, G.; Frampton, C. S. Physicochemical characterization of the orthorhombic polymorph of paracetamol crystallized from solution. *J. Pharm. Sci.* **1998**, *87* (6), 684−693.
(54) Jawerth, L. M.; Münster, S.; Vader, D. A.; Fabry, B.; Weitz, D. A. A blind spot in confocal reflection microscopy: The dependence of fiber brightness on fiber orientation in imaging biopolymer networks. *Biophys. J.* **2010**, *98* (3), L1−L3.